**PAPER • OPEN ACCESS**

# Investigating spatial macroscopic metastability of perovskite solar cells with voltage dependent photoluminescence imaging

To cite this article: George Koutsourakis *et al* 2023 *J. Phys. Energy* **5** 025008

View the article online for updates and enhancements.

# Journal of Physics: Energy

# Investigating spatial macroscopic metastability of perovskite solar cells with voltage dependent photoluminescence imaging

George Koutsourakis[1],[*] [iD], Carys Worsley[2], Michael Spence[2], James C Blakesley[1], Trystan M Watson[2], Matt Carnie[2] and Fernando A Castro[1] [iD]

[1] National Physical Laboratory (NPL), Hampton Road, Teddington, Middlesex TW11 0LW, United Kingdom
[2] SPECIFIC, Swansea University, Bay Campus, Swansea SA1 8EN, United Kingdom
[*] Author to whom any correspondence should be addressed.

E-mail: george.koutsourakis@npl.co.uk

## Abstract

Metastability is a characteristic feature of perovskite solar cell (PSC) devices that affects power rating measurements and general electrical behaviour. In this work the metastability of different types of PSC devices is investigated through current–voltage (*I–V*) testing and voltage dependent photoluminescence (PL-V) imaging. We show that advanced *I–V* parameter acquisition methods need to be applied for accurate PSC performance evaluation, and that misleading results can be obtained when using simple fast *I–V* curves, which can lead to incorrect estimation of cell efficiency. The method, as applied in this work, can also distinguish between metastability and degradation, which is a crucial step towards reporting stabilised efficiencies of PSC devices. PL-V is then used to investigate temporal and spatial PL response at different voltage steps. In addition to the impact on current response, metastability effects are clearly observed in the spatial PL response of different types of PSCs. The results imply that a high density of local defects and non-uniformities leads to increased lateral metastability visible in PL-V measurements, which is directly linked to electrical metastability. This work indicates that existing quantitative PL imaging methods and point-based PL measurements of PSC devices may need to be revisited, as assumptions such as the absence of lateral currents or uniform voltage bias across a cell area may not be valid.

## 1. Introduction

Halide perovskite solar cells (PSCs) were introduced in 2009, with demonstrated efficiencies just below 4% [1]. Since then, PSC efficiencies have grown rapidly, reaching over 25% for single junction cells [2], and over 30% for tandem perovskite-on-silicon devices [3, 4]. Scalability potential towards PSC modules has been demonstrated, with pilot outdoor small scale photovoltaic (PV) systems already being made [5, 6]. Past experience based on organic PV device stability testing protocols has accelerated the understanding of degradation and stability towards more stable PSC devices [7, 8].

The path towards commercialisation of perovskite technology also relies on accurate and reliable power rating of PSC devices. Relevant to power measurements, one of the characteristic features of PSCs is the metastability that is observed when acquiring electrical measurements due to hysteretic behaviour and/or light-soaking effects [9, 10]. Metastability profiles vary between different PSC architectures and materials [11], making it challenging to distinguish between metastability and degradation when measuring the performance of such devices. This presents challenges when applying measurements to accurately determine the power and efficiency of PSC samples, where the choice of *I–V* measurement method may affect results [12].

Several methods have been proposed recently to handle metastability during measurements, and allow accurate and repeatable electrical performance characterisation of PSCs. A dynamic *I–V* curve acquisition approach has been reported, as a straightforward initial approach for more accurate *I–V* acquisition of PSC devices [13, 14]. Asymptotic and maximum power point tracking methods have also been demonstrated as routes towards accurately determining the maximum power ($P_{max}$) and efficiency of PSCs devices [15], with an asymptotic $P_{max}$ scan method presented for performance calibration of perovskite and other emerging PV devices [16]. A protocol where the sweep direction and repeatability of the $P_{max}$ measurement are considered has been proposed recently by the European Solar Test Installation, which makes it possible to distinguish metastability from degradation [17]. Regarding standardised documentation, the IEC TR 63228:2019 serves as a best practice document to provide some guidance for reliable measurements for PSC devices [18].
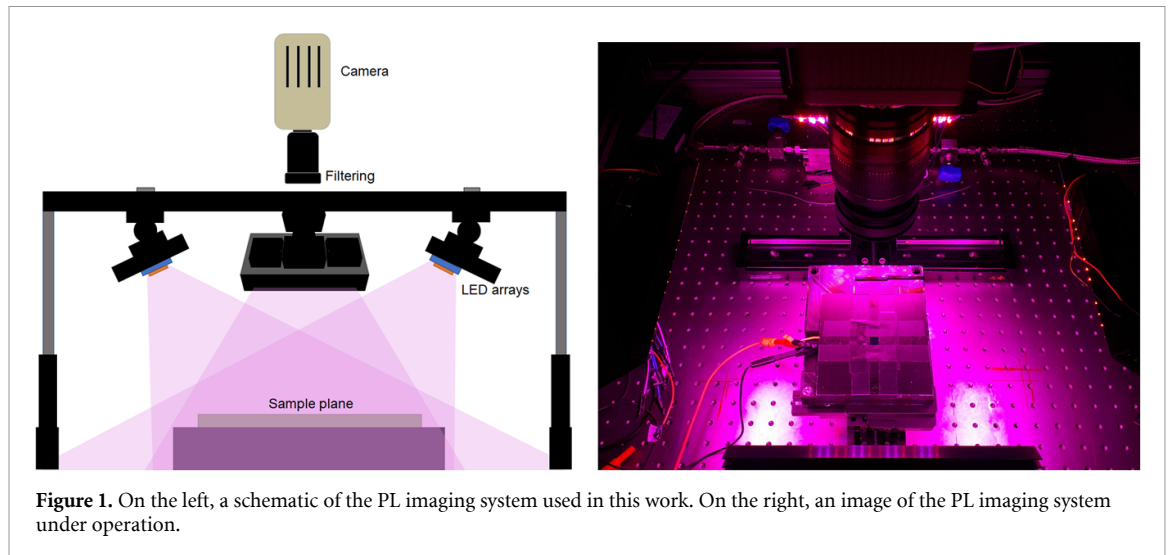
The hysteretic behaviour of PSC devices observed in *I–V* measurements has also been observed in photoluminescence (PL) spectroscopy measurements during voltage changes, attributed to a combination of the electrostatic screening effect and nonradiative recombination effect of ion migration under external electric field [19]. Slow ion migration along with the interactions of these ions with interfaces in PSC devices has been reported as the cause of hysteretic behaviour under applied electric fields [9, 20, 21]. Voltage dependent PL (PL-V) measurements have shown that PL intensity mirrors the current–voltage (*I–V*) measurements in the power-generating range, which allows the study of the correlation between radiative and nonradiative recombination losses [22]. PL spectroscopy has also been demonstrated as a useful technique for the analysis of various steps of PSC device fabrication process and for monitoring crystallisation stages [23, 24]. In addition to bulk PL spectroscopy and PL micro-spectroscopy mapping of PSCs, large area PL imaging has been demonstrated as a fast technique for characterisation of spatial uniformity and stability of PSCs [25–27]. PL imaging presents the advantage of fast measurement speed and the capability to image large areas, full cells and even mini-modules [28], and has been used to analyse the spatially inhomogeneous progression of PSC device performance changes after light-soaking [29]. Routes towards quantitative PL imaging of PSC devices have been demonstrated [30]. As an example, PL imaging at different light or voltage bias levels for PSCs devices has been used to infer spatial charge collection characteristics of transport layers in such devices [31].

In previous studies reported above, PL imaging has been used for spatial characterisation of PSCs, however without taking into account spatial metastability variations of samples, while transient effects or hysteresis have been studied either globally or at specific points of the sample though microscopy methods. In this work, we present for the first time spatial macroscopic metastability effects of PSCs using PL-V imaging. In addition, PL-V imaging is used to investigate spatial metastability effects that take place specifically during maximum power ($P_{max}$) and current–voltage (*I–V*) measurement protocols. This provides a better understanding of what considerations need to be taken during PSC device electrical testing towards standardised measurements. To demonstrate the broad applicability of the approach taken here, measurements have been applied to different types of PSC devices, planar PIN and NIP devices, as well as triple-mesoscopic-layer carbon PSCs. Especially the latter devices demonstrate a very slow response to voltage changes, in the order of seconds, which makes accurate electrical characterisation challenging. *I–V* parameters of such devices are measured, and PL-V imaging is used to monitor the temporal and spatially local PL response of the samples during different voltage steps. Lateral variation of metastability of PSC devices is demonstrated through PL-V measurements, showing that local non-uniformities and defects influence local metastability in PSC devices. Such features can affect reliable *I–V* acquisition and also challenge common assumptions used in quantitative PL imaging, such as voltage bias uniformity across a sample or lack of lateral currents. The combination of imaging methods with measurement of electrical characteristics offers more accurate electrical characterisation of PSC, and also provides insights into how different local defects and non-uniformities impact ion kinetics and thus device metastability.

## 2. Measurement methods and samples

### 2.1. I–V curve acquisition

*I–V* parameters were acquired using fast *I–V* sweeps (forward and reverse in one sweep) with a total time of 20 ms for the whole sweep. Additionally, a variation of the methodology proposed by Bardizza *et al* was used to acquire stabilised *I–V* parameters [17]. During this process, the maximum power point power ($P_{max}$), short circuit current ($I_{SC}$) and open circuit voltage ($V_{OC}$) were tracked until the measured current (or voltage for $V_{OC}$) was stabilised based on a stopping stabilisation criterion, with the sequence $P_{max}$, $I_{SC}$, $P_{max}$, $V_{OC}$, $P_{max}$. This approach allows $P_{max}$ to be recorded towards both forward and reverse bias directions (after $I_{SC}$ tracking and $V_{OC}$ tracking), as well as to monitor if there are stability issues for the sample, while mitigating for metastability [17]. In addition, by recording stabilised values of $I_{SC}$ and $V_{OC}$ a fill factor value
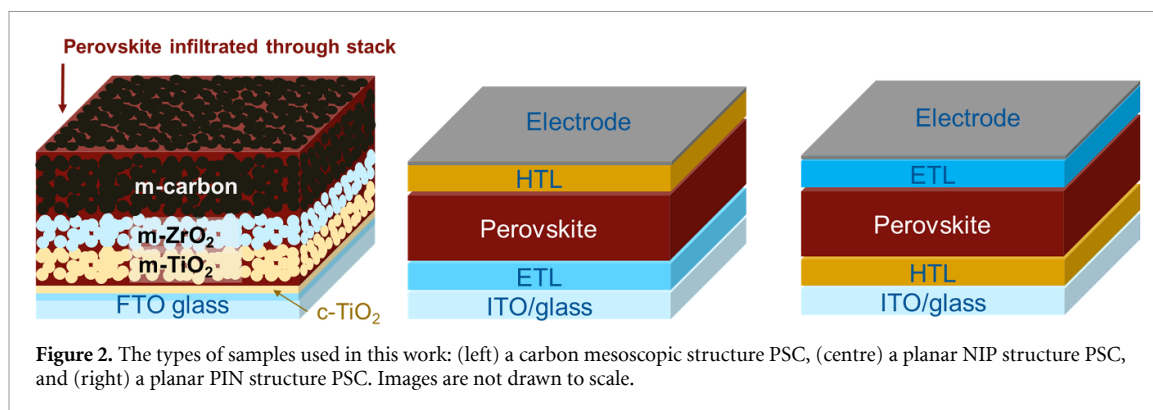
**Figure 1.** On the left, a schematic of the PL imaging system used in this work. On the right, an image of the PL imaging system under operation.

can be obtained. In our variation of this method, no other stabilised points on the $I–V$ curve are recorded apart from $P_{\max}$, $I_{SC}$, and $V_{OC}$ (not considering the tracked points during stabilisation). This helps reduce measurement time significantly for metastable samples. Nevertheless, even the acquisition of these three $I–V$ parameters with the above sequence can last more than 30 min for some samples as will be shown below. The stabilisation criterion selected here to record an $I–V$ parameter point is when current variation during 2 s of continuous sampling is smaller than 0.05% of the mean current value. This is a compromise between total measurement time, avoiding sample degradation, and ensuring repeatability of measurements. Slower metastability effects can take place, which makes the choice of stabilisation criterion dependent on the sample and the user's knowledge about the sample.

All $I–V$ parameter acquisitions were done at standard testing conditions (STCs) for PV devices using a Xe lamp solar simulator (Oriel AAA). A Keithley 2401 sourcemeter was used for acquiring $I–V$ measurements, with an in-house developed LabVIEW program used to control the $I–V$ acquisition, either when applying fast sweeps or when tracking $I–V$ parameters [32]. A temperature controlled chuck with additional temperature feedback from the sample itself was used, although for such long measurement durations the temperature of the active material within the cells might differ from the feedback measured at the glass surface of the sample [33]. A mask of 1 cm $\times$ 1 cm was used for all samples, having the same area as the cell active area. A calibrated KG5-filtered silicon reference cell was used to set the irradiance levels. Preconditioning at STCs for 3 min was applied to all samples before the fast $I–V$ sweep, followed by the $I–V$ parameter tracking.

**2.2. PL-V imaging**

A multispectral excitation, large area PL imaging system has been developed at NPL and was used for this work. The PL imaging system consists of 16 multispectral LED boards; each board includes LEDs of 4 different excitation wavelengths, 380 nm, 450 nm, 625 nm, and 850 nm, with the capability to individually control groups of LEDs of the same wavelength. This allows high irradiance excitation of a range of samples, from semiconductor wafers and single cells of various technologies to tandem samples. The irradiance uniformity at the sample is better than 5% for a 200 mm $\times$ 200 mm area. A Hamamatsu ORCA Flash4.0 CMOS camera is used for capturing images, with a combination of filtering and close-up lenses based on the samples under study. A KG5 calibrated reference cell is used to ensure stable and repeatable irradiance intensity at the sample between measurements of different samples. The system is inside a light-tight enclosure. A schematic and a picture of the system with the blue (450 nm) and red (625 nm) LEDs on are presented in figure 1.

For the PL imaging experiments of this work, a combination of 450 nm and 625 nm wavelength excitation light was used, with its intensity set to induce a 1 sun equivalent current on the KG5 reference cell. A 700 nm longpass filter was used on the camera for all measurements presented in this work, for filtering the LED light and allowing PL emission to be captured. All cells were masked during measurements, with only their active area (1 cm $\times$ 1 cm) exposed. A Keithley 2401 sourcemeter was used for setting the voltage steps and measuring the current response of devices. The schematic of the PL imaging system and a picture of the sample and reference platform under illumination are presented in figure 1. PL images were captured at a 3.3 images s$^{-1}$ rate, while the current was measured during each image acquisition, for the set voltage level.

**Figure 2.** The types of samples used in this work: (left) a carbon mesoscopic structure PSC, (centre) a planar NIP structure PSC, and (right) a planar PIN structure PSC. Images are not drawn to scale.

### 2.3. Samples

Two different types of PSC devices were tested in this work, mesoscopic carbon-based samples and planar (NIP and PIN) samples. A schematic summary of all structures is presented in figure 2. The carbon based mesoscopic PSC samples were based on screen printed layers of mesoporous $TiO_2$, $ZrO_2$, and carbon, with thicknesses of 0.8 $\mu$m, 2 $\mu$m and 12–15 $\mu$m, respectively [34]. Before the layer printing, a compact $TiO_2$ blocking layer ($\sim$50 nm) was deposited on fluorine-doped tin oxide glass at 300 °C by spray pyrolysis of ti(II)-bis-acetylacetonate in isopropyl alcohol (7.5%). The layers were infiltrated with the methylammonium lead iodide ($MAPbI_3$) perovskite precursor solution. Carbon based samples were infiltrated using a mixture of valerolactone and methanol, and the perovskite precursor solution. The perovskite solution also contained 5-aminovaleric acid at 3% (molar) [35].

Planar perovskite cells were all fabricated on indium tin oxide (ITO) coated glass (13 $\Omega/\square$). For PIN cells nickel(II) acetate tetrahydrate (52 mg ml$^{-1}$ in 2-methoxyethanol) was spin coated on the glass at 6000 rpm for 30 s before annealing on a hotplate at 300 °C for 30 min in air. A 1.25 M $MAPbI_3$ solution was deposited by spin coating at 4000 rpm for 30 s and an ethyl acetate anti-solvent was dropped onto the spinning substrate after 6 s, after which the substrates were annealed for 10 min at 100 °C on a hotplate. Phenyl-C61-butyric acid methyl ester ($PC_{61}BM$) (20 mg ml$^{-1}$ in chlorobenzene) followed by bathocuproine (0.5 mg ml$^{-1}$) were deposited by spin coating at 4000 rpm for 20 s. Finally, silver contacts were deposited by thermal evaporation. For NIP cells $SnO_2$ nanoparticles (5% colloidal dispersion in $H_2O$) were spin coated at 4000 rpm for 30 s before annealing at 140 °C for 30 min in air. The perovskite film was produced in the same way as for the PIN architecture. A tetrakis[N,N-di(4-methoxyphenyl)amino]-9,9′-spirobifluorene (spiro-OMeTAD) solution was prepared following the method of Saliba *et al* [36] and dynamically spin coated at 4000 rpm for 20 s to form the hole transport layer. Gold contacts were then deposited by thermal evaporation. To improve stability during characterisation, cells were encapsulated following the method described in Cacovich *et al* [37].

Regarding the samples used in this work: PSC1 is the carbon mesoscopic PSC device, PSC2 the planar PIN PSC device and PSC3 the planar NIP PSC device. Results from a reference GaAs sample are available in the supplementary material, in order to demonstrate the applicability of the methods for a high-performance (closer to an ideal *I–V* response) inorganic cell. Results from additional carbon and planar PSC samples are also included.

## 3. Results and discussion

Initially fast *I–V* sweeps of all samples were acquired, with a total sweep time of 20 ms, including forward and reverse *I–V* curve. Then the *I–V* parameters $P_{max}$ ($\times$3), $I_{SC}$, and $V_{OC}$ were tracked until stabilised, as described in the previous section. *I–V* curves including fast sweeps and tracked parameters are presented in figure 3. The recorded *I–V* parameters are presented in table 1. The fast *I–V* sweep for sample PSC1 exhibits barely any metastability (figure 3(a)). However, when the *I–V* parameters are tracked, it is revealed that the device is metastable, and the initial fast *I–V* parameters would give an inaccurate representation of efficiency since the stabilised $P_{max}$ is $\sim$30% lower than the $P_{max}$ from the fast *I–V*. The device provides a stable $P_{max}$ value as is presented in table 1, after it is tracked three times, with $I_{SC}$ and $V_{OC}$ tracking in-between. PSC2 exhibits both metastability and degradation. Metastability is shown by strong hysteresis in the fast *I–V* sweep and from the tracked stabilised data points being very different from the fast *I–V* points. Degradation of the sample during the measurements is observed during the *I–V* tracking, where the first two $P_{max}$ tracked values (before and after tracking $I_{SC}$) coincide but the last $P_{max}$ tracking step produces a much lower $P_{max}$ value. As it will be observed below, the device also degrades during the corresponding sequence of PL
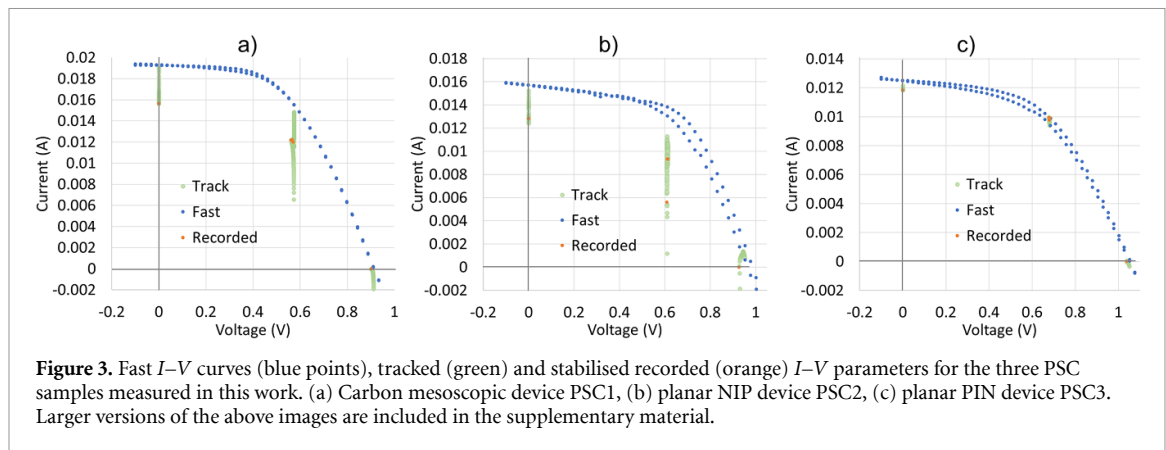
**Figure 3.** Fast *I–V* curves (blue points), tracked (green) and stabilised recorded (orange) *I–V* parameters for the three PSC samples measured in this work. (a) Carbon mesoscopic device PSC1, (b) planar NIP device PSC2, (c) planar PIN device PSC3. Larger versions of the above images are included in the supplementary material.

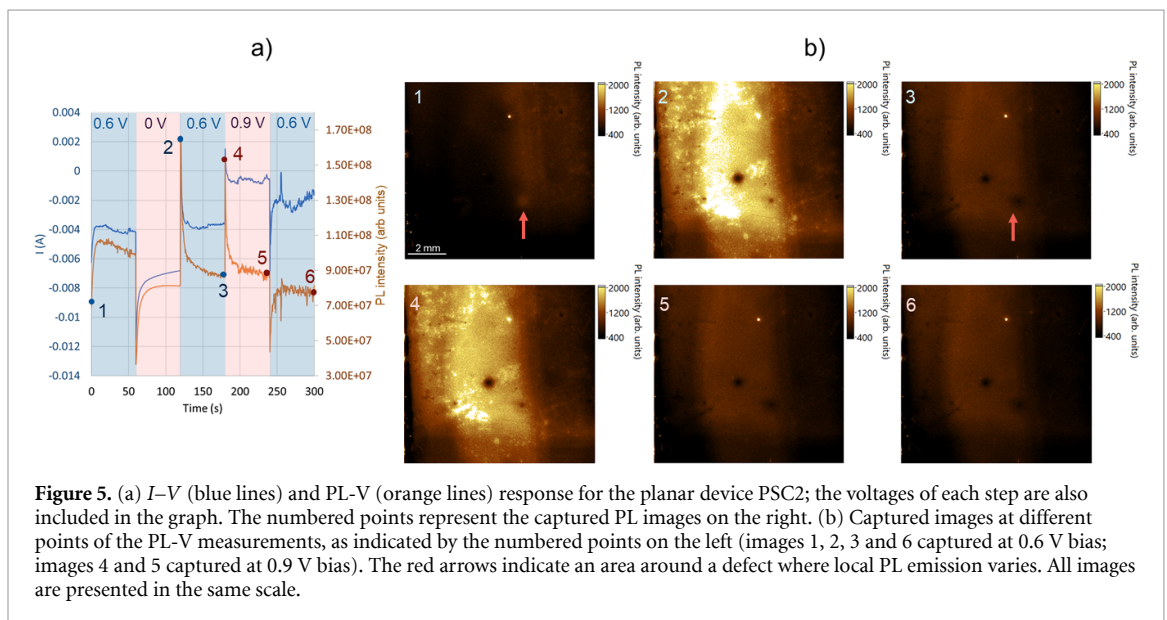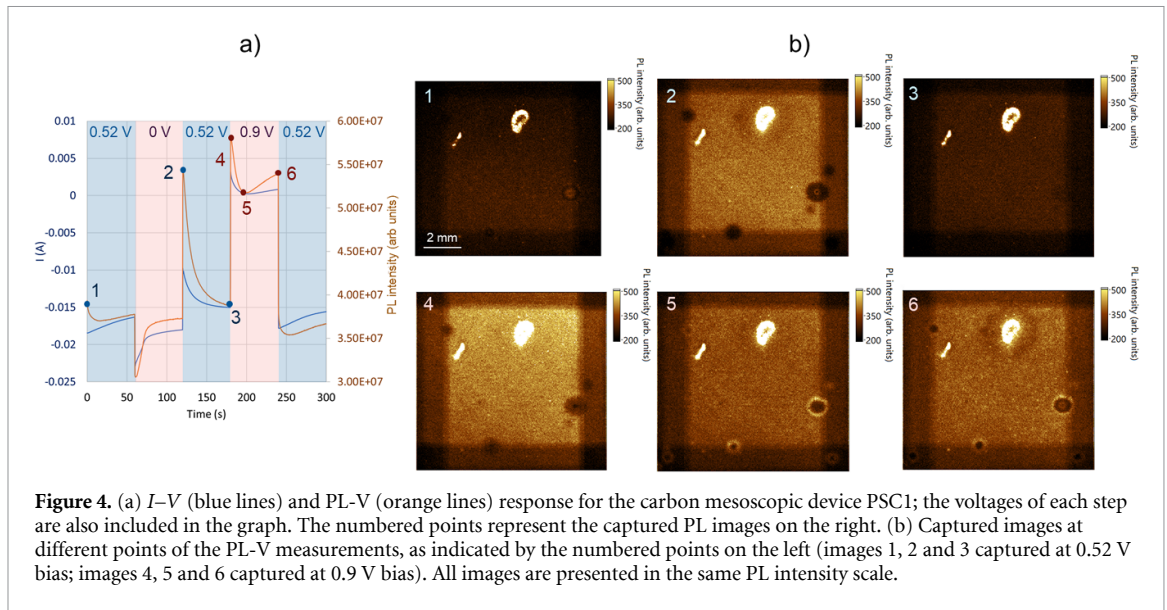**Table 1.** *I–V* data for all samples, both for the tracked *I–V* parameters and for the fast *I–V* sweeps.

| | Recorded (*I–V* parameter tracking) | | | | | Fast | | |
|---|---|---|---|---|---|---|---|---|
| | $P_{max}$ (mW) | | | | | | | |
| Sample | 1 | 2 | 3 | $I_{SC}$ (mA) | $V_{OC}$ (V) | $P_{max}$ (mW) | $I_{SC}$ (mA) | $V_{OC}$ (V) |
| PSC1 | 6.84 | 6.85 | 6.92 | 15.7 | 0.901 | 8.92 | 19.3 | 0.914 |
| PSC2 | 5.71 | 5.72 | 3.41 | 12.8 | 0.926 | 8.8 | 15.7 | 0.965 |
| PSC3 | 6.64 | 6.74 | 6.76 | 11.9 | 1.038 | 6.77 | 12.5 | 1.052 |

imaging measurements. PSC3 presents some metastability in the fast *I–V* curve sweep hysteresis and at $I_{SC}$, whereas $P_{max}$ tracking produces repeatable and stable results that are consistent with the fast *I–V* sweep. Based on the measurements presented here, we find that this measurement approach can provide stabilised $P_{max}$ measurements for metastable perovskite samples whilst also distinguishing between degradation and metastability.

The aim of the above measurements was to study the stability and metastability of the three sample types and (if possible) investigate the stabilised *I–V* parameters of the samples before PL-V imaging. In order to observe spatial variations of metastability, PL images of the samples were measured at the same voltage steps sequence as the recorded values by the *I–V* parameter acquisition above. During these experiments, one image was acquired every 300 ms for each sample, with 1000 images in total, which means multiple images were acquired at each voltage step, in parallel with the current measurement. The different voltage bias steps were applied at specific timing intervals, not necessarily when the measured current of a device was stabilised. The measured current and the total PL emission recorded (integration of the whole image) are presented on the left of figures 4–6 for each sample. As expected, PL emission closely correlates with measured current for all three samples, at different voltage levels. This means that metastability also affects PL emission. On the right of the figures, PL images at specific points in time as marked on the curves are presented, to demonstrate the different temporal variations of PL emission at different areas of each sample, whilst kept at the same voltage level.

For PSC1, the changes in global PL emission are slower for each voltage step than for PSC2 and PSC3, with the device not yet stabilised when the voltage value moves to the next step, as can be observed by the current and PL emission curves (compare figure 4(a), with figures 5(a), and 6(a)). The darker areas at the edges of the sample are the result of shading due to the applied mask on the sample during PL measurements, and its thick front glass. The PL images 1, 2 and 3 in figure 4(b) are all captured at 0.52 V bias, but all demonstrate different spatial behaviour, especially around specific defects. This implies that local defects can affect lateral ion distribution, contributing to metastability. It can also be observed that prior voltage bias conditions have an effect on the behaviour of the device, as can be specifically observed for PL images 2 and 3 in figure 4, which are both at 0.52 V. PL images 4, 5 and 6 are all captured at 0.9 V, and an even more pronounced temporal variation of the spatial PL emission profile can be observed, especially around specific large scale defects in the sample. Such spatial changes affect global PL emission, and consequently induced current, as is also confirmed by the current measurements during PL imaging. Subtraction images between some of these points can be found in the supplementary material, highlighting the differences in spatial profile.

PSC2 is clearly still degrading during PL imaging measurements, as the absolute values of measured current and PL emission are both decreasing throughout all voltage steps, as can be observed in figure 5(a).

**Figure 4.** (a) *I–V* (blue lines) and PL-V (orange lines) response for the carbon mesoscopic device PSC1; the voltages of each step are also included in the graph. The numbered points represent the captured PL images on the right. (b) Captured images at different points of the PL-V measurements, as indicated by the numbered points on the left (images 1, 2 and 3 captured at 0.52 V bias; images 4, 5 and 6 captured at 0.9 V bias). All images are presented in the same PL intensity scale.



**Figure 5.** (a) *I–V* (blue lines) and PL-V (orange lines) response for the planar device PSC2; the voltages of each step are also included in the graph. The numbered points represent the captured PL images on the right. (b) Captured images at different points of the PL-V measurements, as indicated by the numbered points on the left (images 1, 2, 3 and 6 captured at 0.6 V bias; images 4 and 5 captured at 0.9 V bias). The red arrows indicate an area around a defect where local PL emission varies. All images are presented in the same scale.

Despite the degradation behaviour, the device still responds to voltage changes. The results for this device are consistent with the *I–V* parameter tracking, during which the device started degrading during measurements. Images 1, 2, 3 and 6 in figure 5(b) are all captured at 0.6 V, and some local temporal differences in PL emission can be observed. Apart from the apparent differences across large areas in the central and top left parts of image 2, differences around local defects can still be observed in the case of this sample, similar to PSC1. A red arrow in figure 5(b) (images 1 and 3) is used to highlight one local defect, while closer observation can reveal more such local differences in PL emission for the same voltages. There is no observed spatial difference between images 3 and 6, apart from a minor overall reduction in PL emission for the whole sample, as it degrades during measurements. Local differences can also be observed between images 4 and 5, both of which have been captured at 0.9 V. The local differences between the two images are similar to the differences between images 2 and 3, implying that the voltage step direction (lower to higher voltage) has a major effect on metastability, which indicates that it could be related to ionic movement.

PSC3 is also consistent with its *I–V* parameter tracking results, as it demonstrates less pronounced metastability, except for the 1 V bias level, where the current seems to converge rapidly to a stabilised value, but the PL emission still varies through the duration of the voltage step. This is mainly due to the continuous decrease of the PL signal around the defected areas on the right of the sample and at the darker area on the left of the sample (as can be observed in the differential images within the supplementary material). This could be the effect of metastability or degradation, which results in radiative recombination reducing and non-radiative increasing. Since the voltage and current values are stable, charge carrier collection for the
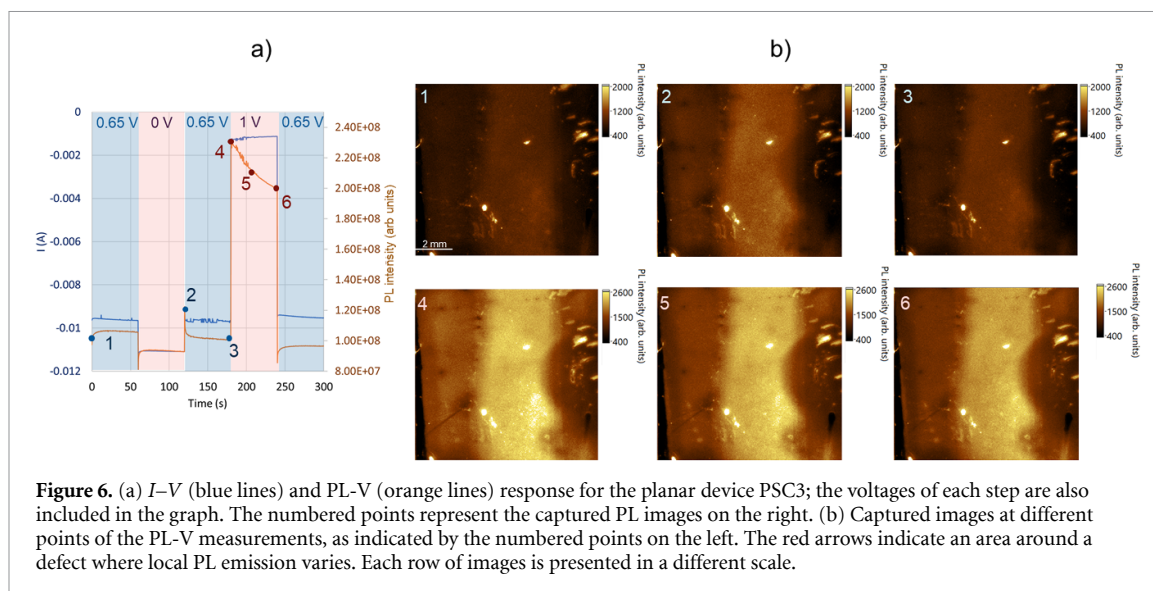
**Figure 6.** (a) *I–V* (blue lines) and PL-V (orange lines) response for the planar device PSC3; the voltages of each step are also included in the graph. The numbered points represent the captured PL images on the right. (b) Captured images at different points of the PL-V measurements, as indicated by the numbered points on the left. The red arrows indicate an area around a defect where local PL emission varies. Each row of images is presented in a different scale.

whole device remains stable, which means the change in PL indicates changes in recombination processes. The sample responds at much faster timescales than the previous two samples, especially compared to the stable PSC1 sample. As can be observed in figure 6(a), the current during the last voltage step of 0.65 V demonstrates an overall minor decrease (in absolute value) compared to the first 0.65 V step (initial 60 s), with an equivalent reduction of total PL emission. This implies a metastability effect is taking place for the whole device, with the short monitoring window not being enough to determine if the initial current will be recovered eventually or if there is degradation also taking place. PL images of the PSC3 device demonstrate general non-uniformities, but metastability effects for this sample are more global than local, or they occur in timescales much shorter than the temporal resolution applied in these measurements.

The mesoscopic PSC1 consists of much thicker active layers than the planar PSC2 and PSC3, and its structure inevitably leads to a much higher defect density than the planar samples. This leads to a slower response in most cases, due to more pronounced metastability effects, observed in the *I–V* parameter acquisition and PL-V measurements. This also allows temporal lateral metastability to be observed using the PL-V method above, which is less effective for observation of such effects on planar devices. Lateral metastability effects are still visible for planar devices and can be more pronounced in the presence of local defects, however they take place on faster timescales than in mesoscopic samples. These results also imply that improvement of sample quality and reduction of local defects in perovskite devices can reduce lateral and, as a result, global metastability effects. Non-uniformities in the observed PL images of this work can be a result of various reasons, from local differences in microstructure, local defects of various layers, or even thickness non-uniformities of the various layers of the devices. Although it is unclear whether the metastability effects observed are due to either the perovskite layer itself, or the different transport layers, we note that all perovskite samples measured in this work demonstrated either metastabilities or degradation effects, or both, during measurements.

Another feature visible in all samples is that even at $I_{SC}$ conditions, there is still some PL signal, indicating that not all carriers are collected, as one would expect for an ideal solar cell. Therefore PL-V measurements can help identify optimised high efficiency samples that demonstrate low metastability and close to ideal behaviour, similar to the behaviour of the reference GaAs sample in the supplementary material. Recent work at a nano- to micro-scale level has demonstrated that photoinduced spatial imbalance in charge accumulation leads to the formation of a lateral space charge distribution and, in some cases, induces degradation [38]. Currently, we cannot be certain if this contributes to the larger-scale lateral variation in metastability observed here. A dedicated future work would be required to understand the physics behind the local defects and why they impact lateral metastability, which is out of the scope of this paper.

An additional implication of these results is that the route towards accurate power rating methods for PSC devices should include control over the operating history of a device before measurement. This is indicated by the temporal PL-V results, where it is apparent that voltage history affects metastability and as a result the $P_{max}$ measurements. As shown in this work, methods similar to the steps used here can produce repeatable measurement results for metastable devices while reliably distinguishing between degradation and metastability effects of PSCs. Local metastability effects should also be considered when quantitative PL imaging is applied. Laterally-resolved metastability effects can be observed in this work, which means that

assumptions applied for quantitative PL imaging methods, such as uniformity of voltage bias or lateral current values, may not be valid in the case of different lateral ion distributions during PL measurement acquisition for a given voltage bias. Similarly, global and lateral metastability effects should be considered when applying other spatial characterisation methods, such us photocurrent mapping or electroluminescence imaging.

## 4. Conclusions

Metastability is a characteristic feature of PSC devices that affects power rating measurements and general electrical behaviour. In this work the metastability of different types of PSC devices has been investigated through *I–V* testing and PL imaging. It has been shown that appropriate *I–V* parameter acquisition methods need to be applied for accurate PSC performance evaluation, and different results are obtained when using simple fast *I–V* curves, which can lead to incorrect estimation of cell efficiency. In addition, advanced *I–V* parameter acquisition methods, as applied in this work, can distinguish between metastability and degradation, which is a crucial step towards reporting stabilised efficiencies of PSC devices.

PL-V imaging has been used to investigate the spatial metastability effects observed during the *I–V* parameter measurements used in this work, which essentially correspond with the voltage steps between $P_{\max}$, $I_{SC}$ and $V_{OC}$. It can be observed that macroscopic, laterally resolved metastability effects take place during electrical bias, with the lateral variation observed mainly around local defects and non-uniform areas of samples. The carbon-based mesoscopic PSC sample demonstrates the most intense metastability effects, which implies that thicker samples with higher defect density demonstrate stronger metastability. The results also indicate that improving fabrication techniques towards higher quality PSC devices will reduce lateral metastability effects, reducing overall global metastability of a sample. Finally, the results presented show that accurate power rating methods for PSC devices need to consider sample bias history for accurate results, especially for distinguishing between metastability and degradation. Laterally varying metastability effects demonstrated here indicate that existing quantitative PL imaging methods and point-based PL measurements of PSC devices should be revisited, as assumptions such as the absence of lateral currents or uniform voltage bias across a cell area may not be valid.

## Data availability statement

The data that support the findings of this study are available upon reasonable request from the authors.

## Acknowledgments

## Author contributions

Conceptualization, G K; methodology, G K; software and system development, G K, J B; sample preparation, C W, M S; measurements, G K; analysis, G K; writing—original draft preparation, G K; writing—review and editing, G K, J C B, C W, M S, T M W, M C, F A C; visualizations, G K; funding acquisition, F A C, T M W, M C.

## ORCID iDs

George Koutsourakis ⬤ https://orcid.org/0000-0002-5552-1749
Fernando A Castro ⬤ https://orcid.org/0000-0002-2409-8300

## References

[1] Kojima A, Teshima K, Shirai Y and Miyasaka T 2009 Organometal halide perovskites as visible-light sensitizers for photovoltaic cells *J. Am. Chem. Soc.* **131** 6050–1
[2] Jeong J *et al* 2021 Pseudo-halide anion engineering for α-FAPbI$_3$ perovskite solar cells *Nature* **592** 381–5
[3] EPFL New world records: perovskite-on-silicon-tandem solar cells (available at: https://actu.epfl.ch/news/new-world-records-perovskite-on-silicon-tandem-sol/) (Accessed 2022)
[4] NREL Best Research-Cell Efficiency Chart (available at: www.nrel.gov/pv/cell-efficiency.html) (Accessed 2022)
[5] De Rossi F *et al* 2018 All printable perovskite solar modules with 198 cm$^2$ active area and over 6% efficiency *Adv. Mater. Technol.* **3** 1800156

[6] Pescetelli S *et al* 2022 Integration of two-dimensional materials-based perovskite solar panels into a stand-alone solar farm *Nat. Energy* **7** 597–607

[7] Reese M O *et al* 2011 Consensus stability testing protocols for organic photovoltaic materials and devices *Sol. Energy Mater. Sol. Cells* **95** 1253–67

[8] Khenkin M V *et al* 2020 Consensus statement for stability assessment and reporting for perovskite photovoltaics based on ISOS procedures *Nat. Energy* **5** 35–49

[9] Snaith H J, Abate A, Ball J M, Eperon G E, Leijtens T, Noel N K, Stranks S D, Wang J T-W, Wojciechowski K and Zhang W 2014 Anomalous hysteresis in perovskite solar cells *J. Phys. Chem. Lett.* **5** 1511–5

[10] Unger E L, Hoke E T, Bailie C D, Nguyen W H, Bowring A R, Heumüller T, Christoforo M G and McGehee M D 2014 Hysteresis and transient behavior in current–voltage measurements of hybrid-perovskite absorber solar cells *Energy Environ. Sci.* **7** 3690–8

[11] Wu F, Bahrami B, Chen K, Mabrouk S, Pathak R, Tong Y, Li X, Zhang T, Jian R and Qiao Q 2018 Bias-dependent normal and inverted J-V hysteresis in perovskite solar cells *ACS Appl. Mater. Interfaces* **10** 25604–13

[12] Dunbar R B *et al* 2017 How reliable are efficiency measurements of perovskite solar cells? The first inter-comparison, between two accredited and eight non-accredited laboratories *J. Mater. Chem.* A **5** 22542–58

[13] Dunbar R B, Moustafa W, Pascoe A R, Jones T W, Anderson K F, Cheng Y-B, Fell C J and Wilson G J 2017 Device pre-conditioning and steady-state temperature dependence of CH₃NH₃PbI₃ perovskite solar cells *Prog. Photovolt., Res. Appl.* **25** 533–44

[14] Gao Q, Lau C F J, Lee E and Monokroussos C 2019 Test method of current-voltage characterisation of perovskite PV module *36th European Photovoltaic Solar Energy Conf. and Exhibition* (*Marseille*) pp 866–73

[15] Song T, Ottoson L, Gallon J, Friedman D J and Kopidakis N 2021 Reliable power rating of perovskite PV modules *2021 IEEE 48th Photovoltaic Specialists Conf. (PVSC)* (IEEE) pp 0367–71

[16] Song T, Friedman D J and Kopidakis N 2021 Comprehensive performance calibration guidance for perovskites and other emerging solar cells *Adv. Energy Mater.* **11** 0–16

[17] Bardizza G, Müllejans H, Pavanello D and Dunlop E D 2021 Metastability in performance measurements of perovskite PV devices: a systematic approach * *J. Phys. Energy* **3** 021001

[18] International Electrotechnical Commission 2019 *IEC TR 63228:2019 Measurement Protocols For Photovoltaic Devices Based On Organic, Dyesensitized Or Perovskite Materials* (available at: https://webstore.iec.ch/publication/64040)

[19] Xu Z, De Rosia T and Weeks K 2017 Photoluminescence–voltage (PL–V) hysteresis of perovskite solar cells *J. Phys. Chem.* C **121** 24389–96

[20] Pockett A and Carnie M J 2017 Ionic influences on recombination in perovskite solar cells *ACS Energy Lett.* **2** 1683–9

[21] Walsh A and Stranks S D 2018 Taking control of ion transport in halide perovskite solar cells *ACS Energy Lett.* **3** 1983–90

[22] Stolterfoht M, Le Corre V M, Feuerstein M, Caprioglio P, Koster L J A and Neher D 2019 Voltage-dependent photoluminescence and how it correlates with the fill factor and open-circuit voltage in perovskite solar cells *ACS Energy Lett.* **4** 2887–92

[23] Mahon N S, Korolik O V, Khenkin M V, Arnaoutakis G E, Galagan Y, Soriūtė V, Litvinas D, Ščajev P, Katz E A and Mazanik A V 2020 Photoluminescence kinetics for monitoring photoinduced processes in perovskite solar cells *Sol. Energy* **195** 114–20

[24] Wagner L, Mundt L E, Mathiazhagan G, Mundus M, Schubert M C, Mastroianni S, Würfel U, Hinsch A and Glunz S W 2017 Distinguishing crystallization stages and their influence on quantum efficiency during perovskite solar cell formation in real-time *Sci. Rep.* **7** 14899

[25] Hameiri Z, Mahboubi Soufiani A, Juhl M K, Jiang L, Huang F, Cheng Y-B, Kampwerth H, Weber J W, Green M A and Trupke T 2015 Photoluminescence and electroluminescence imaging of perovskite solar cells *Prog. Photovolt., Res. Appl.* **23** 1697–705

[26] Soufiani A M, Tayebjee M J Y, Meyer S, Ho-Baillie A, Sung Yun J, McQueen R W, Spiccia L, Green M A and Hameiri Z 2016 Electro- and photoluminescence imaging as fast screening technique of the layer uniformity and device degradation in planar perovskite solar cells *J. Appl. Phys.* **120** 035702

[27] Koutsourakis G, Cao Y, Li B, Jayawardena K D G I, Bandara R M I, Wood S, Blakesley J C, Zhang W, Silva S R P and Castro F A 2019 *In situ* metrology for degradation studies of perovskite solar cells *36th European Photovoltaic Solar Energy Conf. and Exhibition* (*Marseille*) pp 629–33

[28] Ritzer D B, Abzieher T, Basibüyük A, Feeney T, Laufer F, Ternes S, Richards B S, Bergfeld S and Paetzold U W 2022 Upscaling of perovskite solar modules: the synergy of fully evaporated layer fabrication and all-laser-scribed interconnections *Prog. Photovolt., Res. Appl.* **30** 360–73

[29] Soufiani A M, Hameiri Z, Meyer S, Lim S, Tayebjee M J Y, Yun J S, Ho-Baillie A, Conibeer G J, Spiccia L and Green M A 2017 Lessons learnt from spatially resolved electro- and photoluminescence imaging: interfacial delamination in CH₃NH₃PbI₃ planar perovskite solar cells upon illumination *Adv. Energy Mater.* **7** 1602111

[30] Planes E, Spalla M, Juillard S, Perrin L and Flandin L 2019 Absolute quantification of photo-/electroluminescence imaging for solar cells: definition and application to organic and perovskite devices *ACS Appl. Electron. Mater.* **1** 2489–501

[31] Dasgupta A *et al* 2022 Visualizing macroscopic inhomogeneities in perovskite solar cells *ACS Energy Lett.* **7** 2311–22

[32] Mohiuddin T, Nawrocki M and Bitter R 2006 *LabVIEW: Advanced Programming Techniques* (Boca Raton: CRC press) (https://doi.org/10.1201/9780849333255)

[33] Cao Y, Koutsourakis G, Sutton G J M, Kneller J W E, Wood S, Blakesley J C and Castro F A 2019 *In situ* contactless thermal characterisation and imaging of encapsulated photovoltaic devices using phosphor thermometry *Prog. Photovolt., Res. Appl.* **27** 673–81

[34] Meroni S M P, Worsley C, Raptis D and Watson T M 2021 Triple-mesoscopic carbon perovskite solar cells: materials, processing and applications *Energies* **14** 386

[35] Worsley C *et al* 2022 Green solvent engineering for enhanced performance and reproducibility in printed carbon-based mesoscopic perovskite solar cells and modules *Mater. Adv.* **3** 1125–38

[36] Saliba M, Correa-Baena J-P, Wolff C M, Stolterfoht M, Phung N, Albrecht S, Neher D and Abate A 2018 How to make over 20% efficient perovskite solar cells in regular (n–i–p) and inverted (p–i–n) architectures *Chem. Mater.* **30** 4193–201

[37] Cacovich S, Ciná L, Matteocci F, Divitini G, Midgley P A, Di Carlo A and Ducati C 2017 Gold and iodine diffusion in large area perovskite solar cells under illumination *Nanoscale* **9** 4700–6

[38] Richheimer F *et al* 2022 Ion-driven nanograin formation in early-stage degradation of tri-cation perovskite films *Nanoscale* **14** 2605–16